Nuclear Science and Techniques (2025) 36:41
https://doi.org/10.1007/s41365-024-01618-8

Design of a LYSO crystal electromagnetic calorimeter for dark photon detection in the DarkSHINE experiment

Zhi-Yu Zhao[1,2,3] · Qi-Bin Liu[1,2,3] · Ji-Yuan Chen[1,2,3] · Jing Chen[1,2,3] · Jun-Feng Chen[4,5] · Xiang Chen[2,3] · Chang-Bo Fu[6,7] · Jun Guo[2,3] · Kim Siang Khaw[1,2,3] · Liang Li[2,3] · Shu Li[1,2,3] · Dan-Ning Liu[1,2,3] · Kun Liu[1,2,3] · Si-Yuan Song[1,2,3] · Tong Sun[1,2,3] · Jian-Nan Tang[2,3] · Yu-Feng Wang[1,2,3] · Zhen Wang[1,2,3] · Wei-Hao Wu[2,3] · Hai-Jun Yang[1,2,3] · Yu-Ming Lin[1,2,3] · Rui Yuan[1,2,3] · Yu-Lei Zhang[2,3] · Yun-Long Zhang[8,9] · Bai-Hong Zhou[1,2,3] · Xu-Liang Zhu[1,2,3] · Yi-Fan Zhu[1,2,3]

Received: 29 July 2024 / Revised: 14 October 2024 / Accepted: 21 October 2024 / Published online: 28 January 2025

Abstract
This paper presents the design and optimization of a lutetium yttrium oxyorthosilicate (LYSO) crystal electromagnetic calorimeter (ECAL) for the DarkSHINE experiment, which aims to identify dark photons as potential mediators of dark forces. The ECAL design was evaluated through comprehensive simulations, focusing on optimizing dimensions, material selection, energy distribution, and energy resolution. The configuration consisted of 21×21×11 LYSO crystals, each measuring 2.5 cm×2.5 cm×4 cm, arranged in a staggered layout to enhance signal detection efficiency. A 4 GeV energy dynamic range was established to ensure accurate energy measurements without saturation, which is essential for background rejection and signal identification. A detailed digitization model was developed to simulate scintillation, silicon photomultiplier, and analog-to-digital converter behaviors, providing a realistic representation of the detector's performance. Additionally, the study assessed radiation damage in the ECAL region, emphasizing the importance of using radiation-resistant scintillators and silicon sensors.

Keywords Electromagnetic calorimeter · LYSO · Scintillator detector · Light dark matter · Dark photon

1 Introduction

Dark matter (DM) [1, 2] remains one of the most compelling mysteries in cosmology and particle physics, as demonstrated by its gravitational effects on visible matter and the cosmic microwave background. Theoretical models suggest that DM was produced through thermal processes in the early universe, with the "freeze-out" mechanism [3] explaining its current observed density and positing a probable mass range from a few MeV to several TeV. Despite extensive research, the specific properties and particle characteristics of DM remain undefined. Experiments such as XENONnT [4], PandaX [5], CDEX [6], LUX-ZEPLIN [7], AMS [8], DAMPE [9], and LHC [10] have narrowed the parameter space for weakly interacting massive particles (WIMPs) [11–17] in the GeV to TeV range; however, these particles remain undetected [18].

The absence of evidence for high-mass DM candidate particles has increased interest in the sub-GeV mass range, presenting significant detection challenges due to the minimal interaction cross-sections of such light particles with ordinary matter. This necessity has driven the development of innovative detection techniques distinct from traditional DM detection methods. Accelerator-based experiments are particularly promising; they leverage high-energy particle collisions to produce and detect dark photons, which are hypothetical mediators between visible and dark matter [19–23]. Facilities such as NA64 at CERN [24], LHC [25],

Zhi-Yu Zhao, Qi-Bin Liu, and Kun Liu contributed equally to this work.

This work was supported by National Key R&D Program of China (Nos. 2023YFA1606904 and 2023YFA1606900), National Natural Science Foundation of China (No. 12150006), Shanghai Pilot Program for Basic Research–Shanghai Jiao Tong University (No. 21TQ1400209), and National Center for High-Level Talent Training in Mathematics, Physics, Chemistry, and Biology.

Extended author information available on the last page of the article

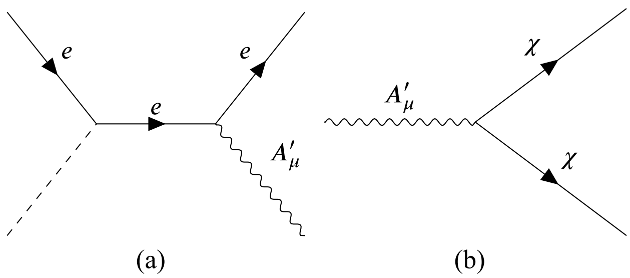

Fig. 1 **a** Production of dark photons via bremsstrahlung. **b** Decay of dark photons into "invisible" modes, resulting in dark matter particles. [29]

BELLE-II [26], BES-III [27, 28], already have results in the search for dark photons [29], and the proposed LDMX [30–32] experiments aim to explore these possibilities.

The DarkSHINE experiment [33, 34], designed to operate under a minimal dark photon model, introduces an innovative approach for detecting these elusive particles. Figure 1 illustrates the conceptual mechanism of dark photon production via dark bremsstrahlung and its subsequent decay into invisible dark matter, forming the experimental basis for DarkSHINE. This experiment leverages the high-repetition-rate single-electron beam provided by the Shanghai High Repetition-Rate XFEL and Extreme Light Facility (SHINE) [35, 36], optimized for detecting subtle signals indicative of dark photons.

This study delineates the design principles of an electromagnetic calorimeter (ECAL) for the DarkSHINE experiment, focusing on material selection and structural layout. Through simulations, the ECAL volume was optimized to balance signal efficiency and cost-effectiveness, and the dynamic range of energy measurements in the ECAL channels was examined. Insights from these analyses informed the development of potential triggering strategies for future detectors. To ensure that the simulated detector response closely reflects real detector behavior, a digitization model was implemented, and the energy resolution of the ECAL was analyzed. Furthermore, we evaluated radiation damage in the ECAL region, emphasizing the importance of crystals and silicon sensors capable of maintaining high performance in high-radiation environments.

2 DarkSHINE experiment and ECAL design

DarkSHINE is a fixed-target experiment designed to study the bremsstrahlung production of dark photons and measure their invisible decay. It uses a high-repetition-rate single-electron beam provided by SHINE and is currently under construction. The beam is expected to reach an energy of 8 GeV and a repetition rate of 10 MHz, corresponding to 3×10^{14} electron-on-target events during the year of the DarkSHINE experiment's commissioning.

The primary challenge for DarkSHINE is integrating data from various detectors to minimize background contributions while preserving the dark photon signal. Figure 2 illustrates the DarkSHINE detector system, comprising a tungsten target and three subdetectors: a tracker, an ECAL, and a hadronic calorimeter (HCAL). Simulations incorporated a single-electron beam with a 3 cm spatial distribution radius and a maximum non-uniform magnetic field of 1.5 Tesla in the tracker region. The tracker, made up of 13 silicon strip layers, measured the momentum and trajectory of electrons. Seven layers were positioned in front of the target to tag (tagging tracker) to tag the incident electron, and six layers were placed behind the target (recoil tracker). A tungsten target (0.1 X_0) was sandwiched between the tagging and recoil trackers. Positioned behind the recoil tracker, the crystal ECAL measures the energy deposited by recoil electrons and photons. Recoil electrons are defined as incident electrons after interaction with or passage through the target. Next, a scintillator-steel sampling HCAL, placed behind the ECAL, captured and vetoed background, particularly neutral hadrons and muons.

To measure the invisible decay of dark photons, precise measurement of the recoil electron energy after each collision is essential to identify any significant energy loss. The

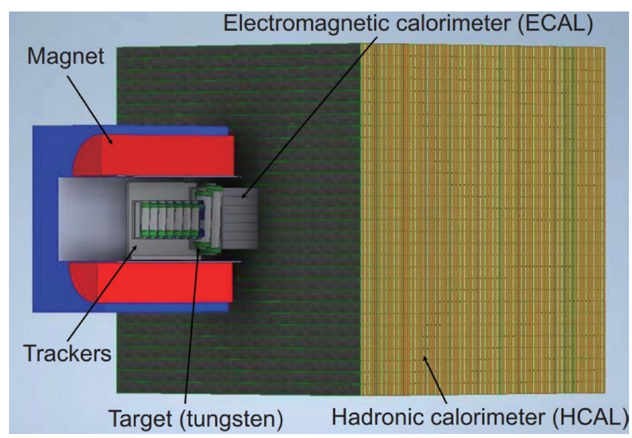

Fig. 2 (Color online) Schematic representation of the DarkSHINE detector system, illustrating the key components involved in the detection of dark photons. The diagram shows the beam entering the center of the detector from the left, traveling along the longitudinal direction. The setup includes a magnet (red) with its supporter (blue), a tagging tracker with seven layers (equal-sized tiles, gray in the middle and green at both ends) inside the magnet, a recoil tracker with six layers (unequal-sized tiles) positioned behind the tagging tracker, and a tungsten target sandwiched between the tagging tracker and the recoil tracker. An electromagnetic calorimeter (small gray cube) is placed behind the recoil tracker, followed by a hadronic calorimeter (large yellow cube) located behind the electromagnetic calorimeter [33]

core detector of DarkSHINE, the ECAL, is a homogeneous LYSO crystal calorimeter. LYSO [37–39] was chosen as the crystal material due to its high light yield, which is critical for achieving excellent electromagnetic resolution, and its rapid scintillation decay time (40 ns), which is crucial for managing the exceptionally high event rate encountered. Furthermore, the ECAL's central region is subject to a significant radiation dose, making radiation resistance an essential property. LYSO demonstrated exceptional durability under high-radiation conditions, making it an optimal choice for the DarkSHINE ECAL.

The structure of the ECAL is illustrated in Fig. 3. The transverse dimensions of ECAL were approximately 52.5 cm×52.5 cm, with a length of about 44 cm along the beam direction, corresponding to approximately 39 radiation lengths. This substantial depth ensures excellent energy containment, allowing the ECAL to absorb nearly all electromagnetic showers and prevent leakage into the HCAL. Preventing such leakage is crucial to avoid the HCAL vetoing dark photon signals. The ECAL volume was determined to balance signal efficiency with crystal cost (Sect. 4). To enhance information collection and improve discrimination of dark photon events, the ECAL was fully segmented. It consisted of 21×21×11 LYSO crystals, each measuring 2.5 cm×2.5 cm×4 cm, covered by ESR, and read out using silicon photomultiplier (SiPMs) [40, 41]. In each layer, the crystals were arranged in a uniform 21×21 grid. To enhance detection efficacy and prevent particles from traversing through gaps, crystals in successive layers were staggered by half the crystal's transverse dimension. This staggered layout aids in detecting recoil electrons with energy loss and capturing dark photon signals [42, 43].

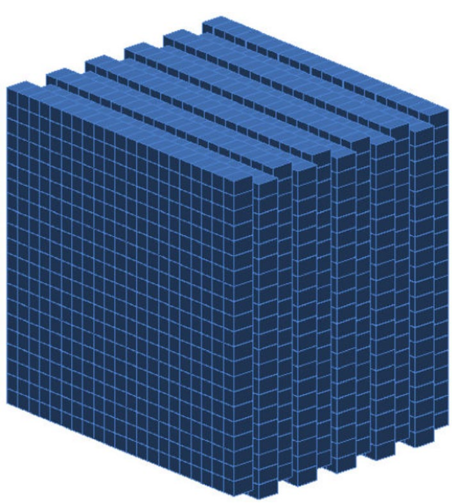

Fig. 3 (Color online) Configuration of the ECAL in DarkSHINE. The ECAL compromises an array of LYSO crystals, each coupled with a single SiPM for readout at the end. The schematic shows the segmentation and staggered layout of the crystals within the ECAL

3 Signal and background

3.1 Software setup

A Monte Carlo simulation of the ECAL was conducted using the DarkSHINE Software (DSS) framework, built on Geant4 [44, 45]. This simulation included the entire detector setup, encompassing the LYSO crystal cubes, wrappers, silicon sensors, support structures, and additional components such as the tracker and HCAL. This comprehensive configuration served as the reference for ECAL reconstruction, while the primary analysis established the appropriate phase space for ECAL evaluation. The DSS framework facilitated the simulation of all Standard Model background processes involving electron–target interactions, as well as various dark photon processes, and their respective detector responses.

The target was used in a "full simulation" scenario, in which an 8 GeV electron beam impacted the target, as outlined in the experimental design, and the resulting secondary particles passed through all detector components. In addition, an "ECAL-unit simulation" was conducted to isolate the response of a single ECAL unit, allowing for detailed analysis of its behavior and facilitating direct comparison with laboratory test results during the R&D phase. All simulations were conducted using consistent material configurations.

3.2 Signal and background

Figure 4 illustrates the background processes accounted for in the DarkSHINE experiment and their relative rates under an 8 GeV electron beam. Typically, incident electrons pass through the target with minimal interaction. Approximately 6.7% of the electrons undergoes hard bremsstrahlung, where bremsstrahlung photons carry more than 4 GeV

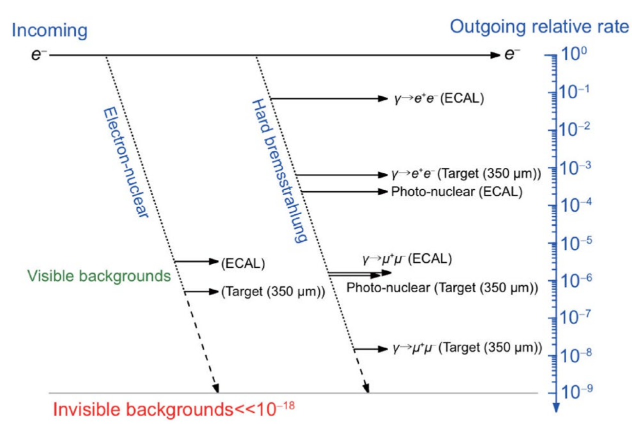

Fig. 4 Background processes observed in the DarkSHINE experiment and their relative rates, simulated under an 8 GeV electron beam

of energy away from the incident electrons. These photons may then interact with the target or ECAL materials via photon-nuclear interactions, which occur at relative rates of 2.31×10^{-4} and 1.37×10^{-6}, respectively. Occasionally, bremsstrahlung photons may convert into muon pairs, with relative rates of 1.63×10^{-6} in the ECAL and 1.50×10^{-8} in the target. Additionally, these photons frequently produce electron–positron pairs. Electron–nuclear interactions within the ECAL and target materials also contribute to the background, with relative rates of 3.25×10^{-6} and 5.10×10^{-7}, respectively [33].

When a dark photon is produced during the electron-on-target process, most of the incident energy transfers to it, while the recoiled electron deposits the residual energy in the ECAL. Dark photons subsequently decay into dark matter, leaving no observable signal in the tracker or calorimeter and resulting in significant energy loss in the ECAL. As depicted in Fig. 5, over 75% of events from 1 MeV dark photon signals exhibit energy deposits below 4 GeV in the ECAL. As the dark photon mass increases, it carries more energy away from the electrons, further enhancing the measured energy loss in the ECAL.

The inclusive process encompasses all potential Standard Model interactions occurring within the detector, weighted by their branching ratios. In comparison to dark photon signals, most events in the inclusive background deposit a substantial portion of their energy in the ECAL, making the total energy measurement in the ECAL a strong criterion on background rejection.

During the inclusive process, hard bremsstrahlung or photon conversion into electron–positron pairs can create electromagnetic showers in the ECAL, leading to significant energy deposition. In contrast, complex processes involving the production of high-energy muon pairs or hadrons generally result in minimal energy deposition in the ECAL and can be effectively filtered out using the tracker and HCAL.

Neutrino-producing background processes, such as Moller scattering ($e^-e^- \rightarrow e^-e^-$) followed by a charged-current quasi-elastic (CCQE) reaction ($e^-p \rightarrow \nu_e n$), neutrino pair production ($e^-N \rightarrow e^-N\nu\nu$), bremsstrahlung with CCQE, and charge-current exchange with exclusive channels ($e^-p \rightarrow \nu n\pi^0$), as outlined in [46], were considered negligible in this experiment due to their low event rates. Consequently, these background processes were excluded from the DarkSHINE simulations [33].

In summary, the design and function of the ECAL focus on excluding backgrounds that do not involve hard muons or hadrons.

4 Volume optimization

As the dark photon mass increases, they carry a larger share of the incident electron's energy, which results in a more significant recoil angle–defined as the angle between the particle momentum direction and the beam axis. Figure 6 illustrates the distribution of recoil angles for particles striking the front surface of the ECAL for both inclusive background events and dark photon signals at different masses. The ECAL spans a cross-sectional area of 52.5 cm×52.5 cm. Inclusive background events predominantly involve electrons that pass through the target and strike near the center of the ECAL, with minor divergences due to the beam's spread and magnetic

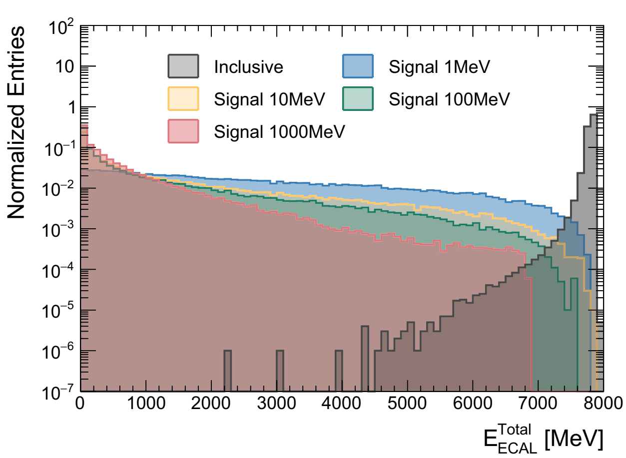

Fig. 5 (Color online) Energy deposition in the ECAL for 8 GeV electrons during dark photon processes and inclusive background interactions. In dark photon events, the deposited energy in the ECAL typically falls below 4 GeV, with energy decreasing as the dark photon mass increases. Conversely, inclusive background processes exhibit substantially higher energy deposition within the ECAL

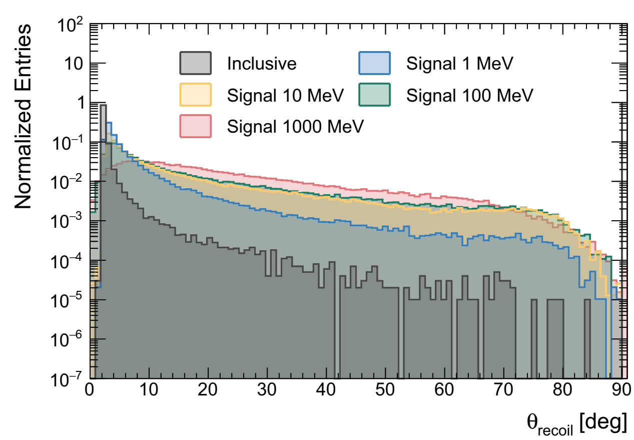

Fig. 6 (Color online) Recoil angle distribution for particles hitting the ECAL in different processes. The recoil angle, defined as the angle between the particle's momentum direction and the beam axis, is shown for both inclusive background processes and dark photon signals. The ECAL has a cross-sectional area of 52.5 cm×52.5 cm. Dark photon signals tend to exhibit larger recoil angles than inclusive background processes, with an increase in dark photon mass resulting in more events impacting the peripheral regions of the ECAL

deflection. Conversely, signal events with dark photons showed wider recoil angle distributions. Higher-mass dark photons are more likely to produce recoil electrons in the ECAL's peripheral region, increasing the chance of missing the ECAL altogether. These cases, however, can be detected and vetoed by the HCAL. Increasing the ECAL size could enhance signal detection efficiency but would also involve balancing with cost considerations.

The signal region of the calorimeter is defined in Table 1. It includes criteria where the total energy deposited in the ECAL is below 2.5 GeV, the total energy in the HCAL is less than 30 MeV, and the maximum energy of a single unit in the HCAL is under 0.1 MeV. This signal region was established to maintain a low background level within 3×10^{14} electron-on-target events. It is derived from a comprehensive analysis of all subdetectors, using specific energy thresholds for the ECAL and other components, along with extrapolation methods to exclude background contributions [33, 47]. The optimization results for the ECAL were evaluated based on signal efficiency, defined as the ratio of the number of events falling within the signal region to the total number of simulated events.

The ECAL size was optimized in both transverse and longitudinal dimensions, with the longitudinal direction aligned along the beam axis. During this optimization process, the individual crystal dimensions were kept constant at 2.5 cm× 2.5 cm×4.0 cm, which was determined based on the maximum density that the electronics can accommodate [48].

First, the transverse dimensions of the ECAL were adjusted while maintaining a constant longitudinal length across the 11 layers. Four distinct calorimeter configurations were simulated. The results presented in Fig. 7a indicate that increasing the transverse size of the ECAL leads to enhanced signal efficiency for various dark photon masses. The average signal efficiency corresponding to all mass points for each calorimeter size is summarized in Table 2.

The width of the ECAL was increased by seven crystal blocks each time. From a design with 14×14×11 crystals to one with 21×21×11 crystals, the ECAL area increased by 2.25 times, resulting in a 17.46% improvement in signal efficiency. However, when the number of crystals per layer reached 35× 35, the increase in signal efficiency became marginal. Considering the cost of the crystals, an ECAL with 21×21 crystals is considered appropriate.

The impact of the detector's longitudinal size on signal efficiency was also investigated. For each volume change, the transverse dimensions of the ECAL were kept constant at 21

Table 1 Defined signal region criteria for the calorimeters in the DarkSHINE experiment

ECAL	HCAL
$E_{\mathrm{ECAL}}^{\mathrm{total}}$ <2.5 GeV	$E_{\mathrm{HCAL}}^{\mathrm{total}} < 30$ MeV, $E_{\mathrm{HCAL}}^{\mathrm{MaxCell}}$ <0.1 MeV

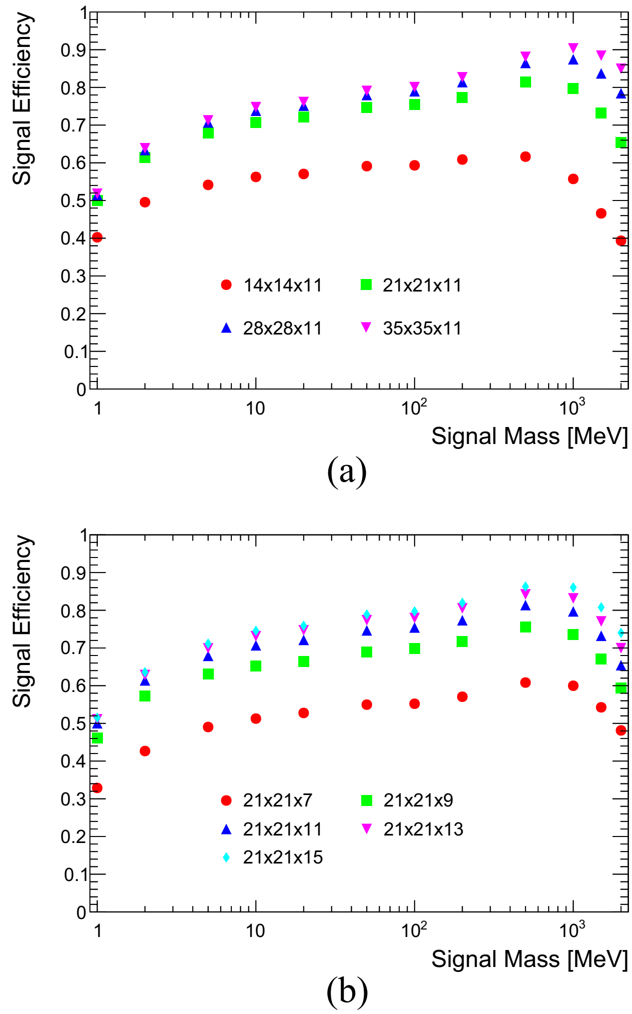

Fig. 7 (Color online) Signal efficiency as a function of dark photon mass for different ECAL configurations. Signal efficiency is defined as the ratio of events entering the signal region (Table 1) to the total number of simulated events. The notations "$x \times y \times z$" in the legends represent the number of crystals in the ECAL along the transverse-x, transverse-y, and longitudinal-z dimensions, with each crystal measuring 2.5 cm×2.5 cm×4.0 cm. Signal efficiency optimization based on (**a**) transverse size variations, illustrating the enhancement of signal efficiency with increased transverse dimensions, particularly for higher dark photon masses. **b** Longitudinal size variations, demonstrating that an increase in longitudinal size improves signal efficiency

Table 2 Average signal efficiency for different transverse sizes of the ECAL

Number of crystals	Average signal efficiency (%)
14×14×11	53.32
21×21×11	70.78
28×28×11	75.75
35×35×11	77.62

Table 3 Average signal efficiency with varying longitudinal size of the ECAL

Number of crystals	Average signal efficiency (%)
21×21×7	52.05
21×21×9	66.32
21×21×11	71.52
21×21×13	74.07
21×21×15	76.71

× 21 crystals, and two layers were added longitudinally, maintaining a consistent number of crystals. As shown in Table 3, the increase in average signal efficiency begins to plateau at 11 layers. Consequently, 11 longitudinal layers were selected as the final configuration.

Overall, an ECAL size of 52.5 cm×52.5 cm×44 cm was chosen, balancing significant signal efficiency with reasonable cost.

5 Energy distribution

In the fixed-target experiment, incident particles that do not undergo significant energy loss predominantly impact the central area of the ECAL, resulting in substantial energy deposition within the crystals in the central region of the initial layers. Additionally, the energy absorbed by crystals varies considerably across different regions; crystals closer to the edges typically experience minimal energy deposition. To determine the dynamic energy range for future detectors and explore potential triggering methods for the ECAL, energy deposition in crystals from various regions was analyzed.

5.1 Energy deposition in different regions

Using the optimized ECAL volume described in Sect. 4, the energy deposition in the crystals for dark photon signals and background processes is shown in Fig. 8. Inclusive background processes typically result in higher energy deposits in the crystals, often up to 4 GeV. In comparison, energy deposition from dark photon signals tends to be slightly lower, with smaller dark photon masses leading to higher energy deposits. A 1 MeV dark photon can deposit up to 3.5 GeV in the crystals, as such dark photons have a low probability of carrying minimal kinetic energy, allowing the recoiling electron to retain most of the incident energy.

The ECAL was divided into four sections from the center to the periphery (Fig. 9) to study energy deposition in different regions. The number of crystals in each region is listed in Table 4. Region-I (red) represents the core area of shower development and contains 125 crystals, each

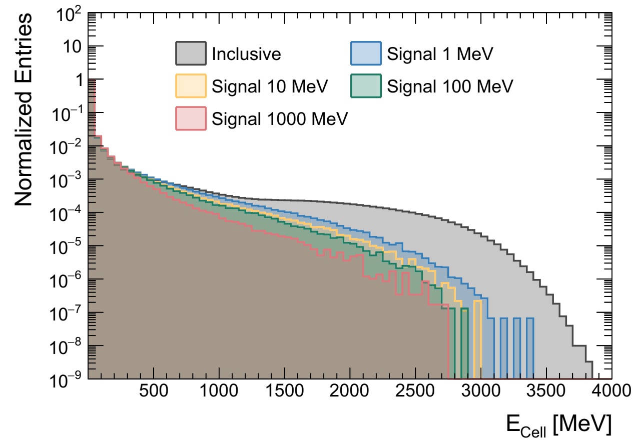

Fig. 8 (Color online) Energy deposited in individual crystals by an 8 GeV electron beam incident on the ECAL. For inclusive background processes, the energy absorbed by a single crystal can reach up to 4 GeV, while dark photon signals can result in energy deposits of up to 3.5 GeV

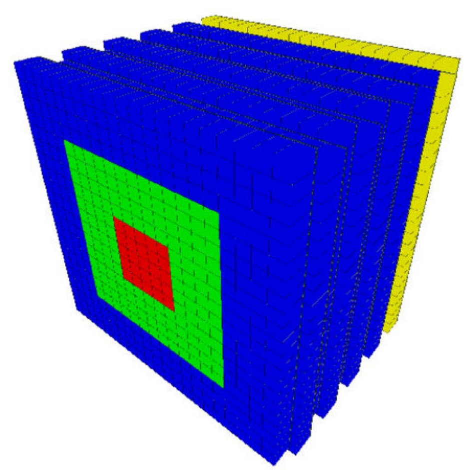

Fig. 9 (Color online) ECAL divided into four regions from the center to the periphery. Red: region-I, green: region-II, blue: region-III, yellow: region-IV. The beam enters the detector at the center, traveling in the longitudinal (z) direction from left to right

Table 4 Number of crystals in each region as depicted in Fig. 9

Dimension	Region-I	Region-II	Region-III	Region-IV
Transverse-x	5	13	21	21
Transverse-y	5	13	21	21
Longitudinal-z	5	7	9	2
Total	125	1058	2786	882

measuring 2.5 cm×2.5 cm×4 cm, roughly equivalent to 18 radiation lengths. This region covers the entire beam spot with a radius of 3 cm, and an additional area equivalent to one Molière radius. The energy absorbed by crystals in each

of these four regions is shown in Fig. 10. Crystals in the central and near-central regions absorb significantly more energy than those in Regions III and IV, which are farther from the shower center and absorb noticeably less energy. For dark photon signals, energy deposition was even lower than that for inclusive background processes. Figure 11 shows that crystals in Region-I, which constitute only 2.6% of the ECAL volume, absorb more than 90% of the energy for inclusive backgrounds.

5.2 Energy limits on channels

The setup of the dynamic energy range is crucial for the accuracy of energy measurements in the ECAL. Typically, a narrower dynamic range results in higher measurement precision. To determine the minimum dynamic range that fulfills the ECAL's energy measurement requirements, an energy cap was applied to each crystal. This cap simulated the saturation behavior seen in real detectors when the deposited energy exceeded the set limit. If this energy limit was too low, it could lead to an overall reduction in the energy recorded by the ECAL, thereby misidentifying high-energy background events as dark photon signals due to significant energy underestimation. The analysis focused on events characterized by substantial energy losses, assessing how different energy limits influenced the count of events where the total energy measured by the ECAL dropped below 4 GeV.

Figure 12 shows the total energy distribution in the ECAL following the application of various energy limits to the channels. As the energy limit decreased below 3 GeV, a notable decline in the total energy measured by the ECAL

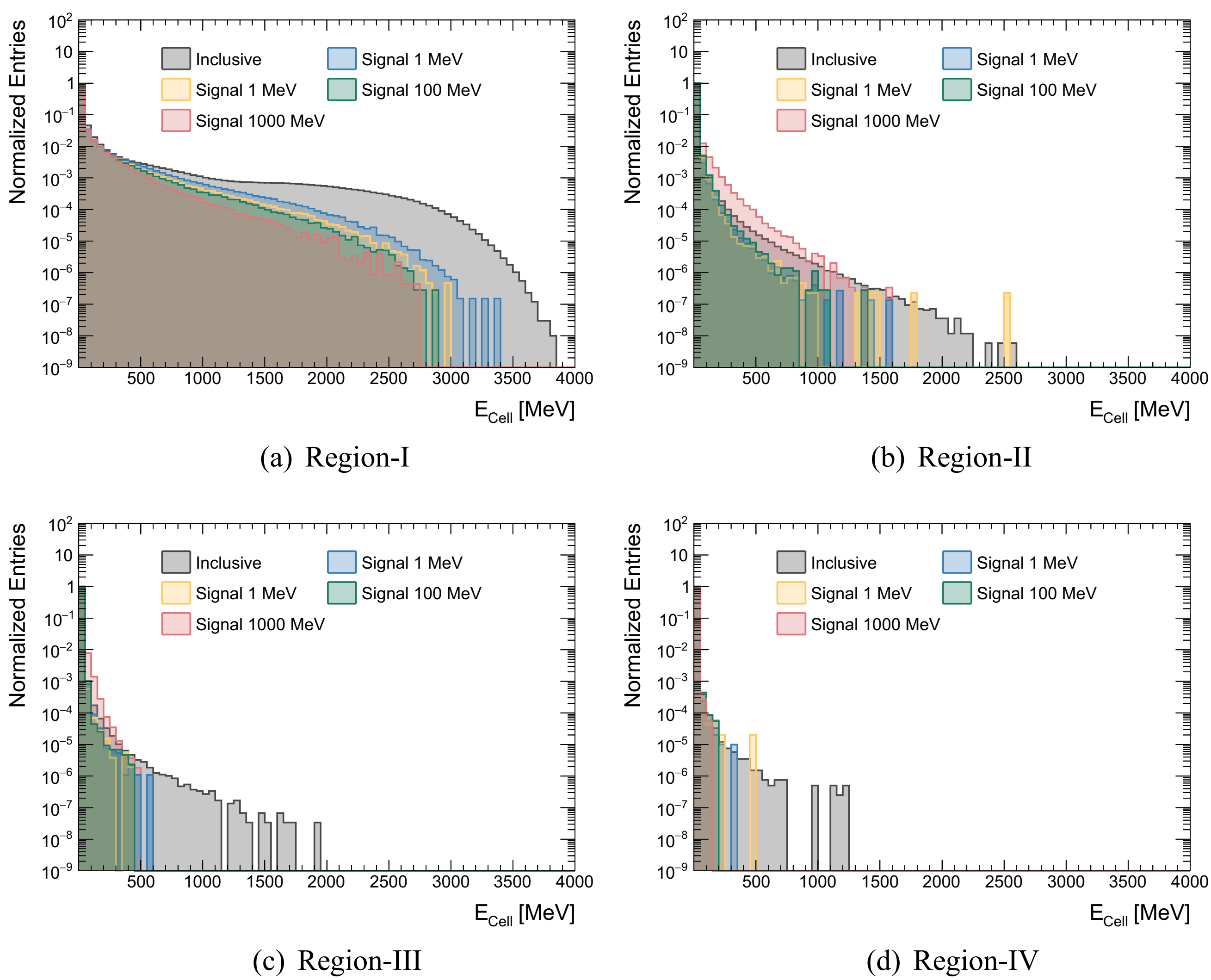

Fig. 10 (Color online) Energy absorbed by single crystals in the four regions shown in Fig. 9. Crystals in the central regions (Region-I and Region-II) absorb significantly more energy, whereas crystals in Region-III and Region-IV, located farther from the shower center, absorb noticeably less energy

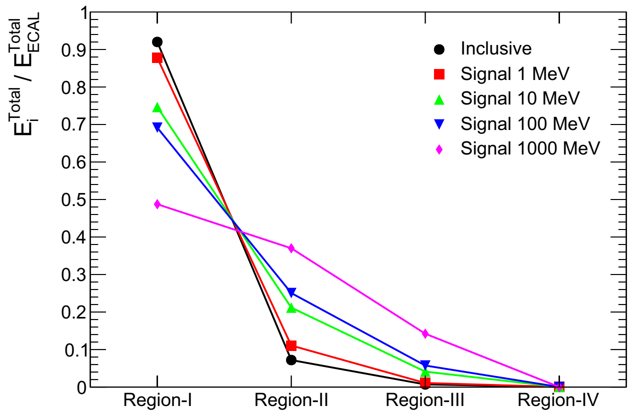

Fig. 11 (Color online) Energy ratio in different regions shown in Fig. 9 for various processes. The energy ratio is defined as the ratio of the total energy deposited in the crystals within a specific region (E_i^{Total}) to the total energy deposited across all crystals in the ECAL ($E_{\mathrm{ECAL}}^{\mathrm{Total}}$). Both signal and background processes deposit the highest energy in Region-I. However, for dark photon processes, as the dark photon mass increases, a greater proportion of the energy is absorbed in the outer regions

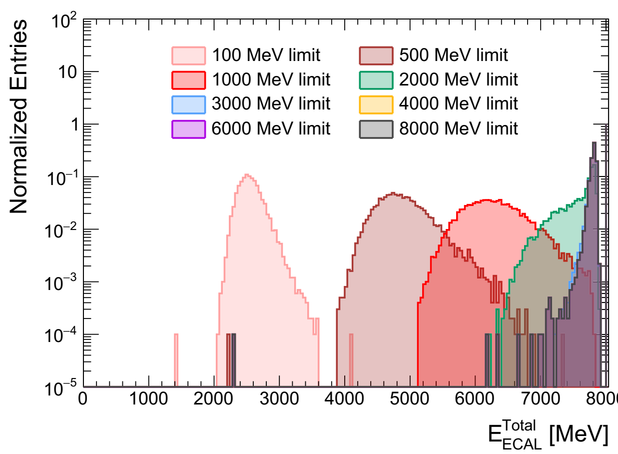

Fig. 12 (Color online) Energy distribution in the ECAL for inclusive background processes after applying various energy limits to individual channels. The energy limit represents the maximum energy that a single channel can record, simulating saturation effects observed in detector electronics. When this limit is set too low, the measured energy in the ECAL can significantly diverse from the actual incident energy, resulting in a shift toward lower energy values. This misrepresentation increases the risk of misidentifying background events as dark photon signals

was observed, which parallels the saturation effect resulting from an inadequate dynamic range in the detector's electronics. When the energy limit exceeded 3 GeV, the total energy recorded by the ECAL remained largely unaffected by the imposed limit. To maintain accurate energy measurements within the ECAL, it is essential that the dynamic range of the individual channels does not compromise the total energy recorded. Consequently, as demonstrated in Fig. 12, a dynamic range exceeding 3 GeV is deemed appropriate.

Table 5 lists the ratios between the number of events with ECAL energies less than 4 GeV and the total number of simulated events. These ratios were derived from background and dark photon signals of varying masses after applying different channel energy limits. As the energy limit decreases, the inclusive background experiences greater energy loss, resulting in an increasing number of cases in which the ECAL energy is less than 4 GeV. The results indicate that a dynamic range of 100 MeV or 500 MeV is insufficient, as these limits exhibit a poor background rejection capability with a statistical sample of one million events. When the energy limit on the channels is set above 500 MeV, nearly all events deposit more than 4 GeV of energy in the ECAL, except for two photon-muon pair processes and one nuclear process, which can be effectively vetoed by the HCAL. This indicates that very few crystals exhibited energy depositions exceeding 1 GeV, as reflected in the normalized entries shown in Fig. 8. Therefore, to ensure effective background rejection, the energy limit should be set to at least 1 GeV.

Overall, a 4 GeV dynamic energy range is optimal for the DarkSHINE ECAL, as it maintains the accuracy required for energy measurements while ensuring strong background rejection capability. Future detector readout electronics can be designed based on this standard.

5.3 Trigger efficiency

In the high-frequency beam environment of DarkSHINE, the majority of events collected by the detector were background events of limited interest. These background events can significantly strain data transmission and storage at the backend. Implementing an online trigger to filter out events that do not match the characteristics of dark photon signals can significantly reduce resource usage. The preliminary trigger design involves summing the energy across selected channels in the ECAL. If the summed energy was less than 4 GeV, the event would be saved. Trigger efficiency is defined as the ratio of the number of triggered events, where the summed energy in the trigger region is less than 4 GeV, to the total number of events. Table 6 lists the trigger efficiencies across the different trigger regions.

In Table 6, a 4 GeV trigger effectively rejects most of the inclusive background, with minimal losses for dark photon signals, particularly those with larger masses. By using only 125 crystals in Region-I, over 99.9% of inclusive background events can be filtered out, thereby conserving resources such as bandwidth and storage. When the summed energy from all crystals in the ECAL is used for triggering, nearly 100% efficiency can be achieved, with only a few rare background processes exhibiting exceptions. This trigger strategy demonstrates significant promise in reducing background events

Table 5 Ratios between the number of events with ECAL energy less than 4 GeV and the total number of simulated events, calculated after applying various channel energy limits to background and dark photon signals of different masses. As the energy limit decreases, the total energy measured by the ECAL also tends to decrease, resulting in an increased number of events within the region where the total ECAL energy is less than 4 GeV

Energy limit	Inclusive	1 MeV dark photon (%)	10 MeV dark photon (%)
100 MeV	999967/1 M	100	100
500 MeV	1066/1 M	90.57	96.93
1000 MeV	3/1 M	76.78	91.23
2000 MeV	3/1 M	76.76	89.89
3000 MeV	3/1 M	76.76	89.89
4000 MeV	3/1 M	76.76	89.89
6000 MeV	3/1 M	76.76	89.89
8000 MeV	3/1 M	76.76	89.89

Energy limit	100 MeV dark photon (%)	1000 MeV dark photon (%)
100 MeV	100	100
500 MeV	98.27	99.5
1000 MeV	94.52	98.56
2000 MeV	93.52	98.32
3000 MeV	93.52	98.32
4000 MeV	93.52	98.32
6000 MeV	93.52	98.32
8000 MeV	93.52	98.32

Table 6 Trigger efficiency across different trigger regions. The trigger efficiency is defined as the ratio of the number of triggered events, where the summed energy in the trigger region is below 4 GeV, to the total number of events. The trigger regions I, II, III, and IV correspond to those shown in Fig. 9

Trigger region	Inclusive	1 MeV dark photon (%)	10 MeV dark photon (%)
No trigger	1 M/1 M	100	100
I	746/1 M	77.57	91.58
I+II	37/1 M	74.05	90.03
I+II+III	6/1 M	73.78	89.9
I+II+III+IV	3/1 M	73.75	89.9

Trigger region	100 MeV dark photon (%)	1000 MeV dark photon (%)
No trigger	100	100
I	94.86	98.75
I+II	93.67	98.35
I+II+III	93.57	98.32
I+II+III+IV	93.57	98.32

while having a negligible impact on dark photon signals, even when relying solely on the channels in Region-I. This study serves as a critical reference for the electronic design of future detectors.

6 Energy resolution

6.1 Energy digitization

Accurate simulation of the detector response requires a precise description of digitization effects. Digitization introduces realistic aspects to simulation results, replicating actual detector behavior and enhancing comparability with real experimental conditions. The energy obtained directly from Geant4, referred to as the truth energy, reflects the ideal energy deposition of a particle in a perfect detection scenario, devoid of detector effects or measurement errors. Thus, digitization provides a more realistic portrayal of detector performance and supports design validation [49, 50].

The primary goal of energy digitization is to parameterize the behavior of each component related to energy measurement, incorporating smearing effects derived from preliminary experiments. For the DarkSHINE ECAL, the energy digitization process consists of three main components: scintillation digitization, SiPM digitization, and analog-to-digital converter (ADC) digitization. These components correspond to the light emission and decay of the scintillator, the SiPM response, and the behavior of the readout electronics, respectively, all based on preliminary experimental measurements.

6.1.1 Scintillation digitization

The first step in the digitization process is scintillation digitization. This phase involves sampling the fluctuations that may occur during the generation and attenuation of scintillation light. We established an intrinsic light yield of 30,000 photons per MeV for the LYSO crystal scintillator, assuming a 10% fluctuation across all scintillators. The scintillation light, which is proportional to the energy deposited in the crystal, is modeled to follow a Poisson distribution. During its propagation within the crystal, scintillation light experiences attenuation, which is influenced by the photon transport length and the photon detection efficiency (PDE) of the SiPM. The measured light yield is crucial for determining the extent of light loss during both propagation and detection. Although the measured light yields for all crystal-SiPM units show fluctuations, they can be calibrated to a certain extent, with an assumed accuracy of 1%. The parameters used in this step are summarized in Table 7.

Table 7 Parameters used in scintillation digitization

Scintillator	Light yield (intrinsic)	Light yield fluctuation
LYSO	30000 ph/MeV	10%
Light yield calibration accuracy		Light yield (measured)
1%		150 p.e./MeV

Table 8 Parameters used in SiPM digitization

Active area (mm^2)	Pixel pitch (μm)	Pixel number
3.0×3.0	10	89984
PDE ($\lambda = \lambda_p$)	Fill factor	Gain fluctuation
18%	31%	10%

6.1.2 SiPM digitization

For SiPM digitization, a toy Monte Carlo model [51] was used to simulate the response of the SiPM to scintillation light from a LYSO crystal. This model was specifically designed to describe the relationship between the number of photons detected by the SiPM and the number of incident photons. The simulation was based on the HAMAMATSU S14160-3010PS datasheet [52], which features a sensitive area of 3 mm× 3 mm, 10 μm pixels, and nearly 90,000 pixels in total, with a LYSO crystal measuring 2.5 cm×2.5 cm× 4 cm. The model accounts for the PDE, pixel density, pixel recovery, and cross talk effects of the SiPM, as well as the scintillation decay time, transmittance, emission spectrum, and absorption spectrum of the LYSO crystal. The parameters used in SiPM digitization are listed in Table 8.

In Fig. 13, N_{fired} represents the number of photons detected by the SiPM, ϵ denotes the PDE of the SiPM, and N_{In} represents the number of photons incident on the SiPM. The SiPM exhibits a nearly linear response when the effective photon count, calculated as the product of the PDE (ϵ) and the number of incident photons (N_{In}), is less than 10,000. As the effective photon count increases, the response gradually deviates from linearity and approaches saturation. A formula from [53] was employed to fit the response of the SiPM, aiding in modeling its behavior for varying numbers of incident photons and providing a means to correct for saturation effects.

In the SiPM digitization, the number of photoelectrons from the scintillation digitization was used as the input for the fitting function shown in Fig. 13, resulting in a response that includes the nonlinear effects of the SiPM. The fluctuations during this process can also be estimated, approximately proportional to the square root of the effective photon count. Furthermore, the inverse of this fitting function can be applied to correct the nonlinear response of the SiPM; however, this correction inevitably reintroduces fluctuations [54, 55].

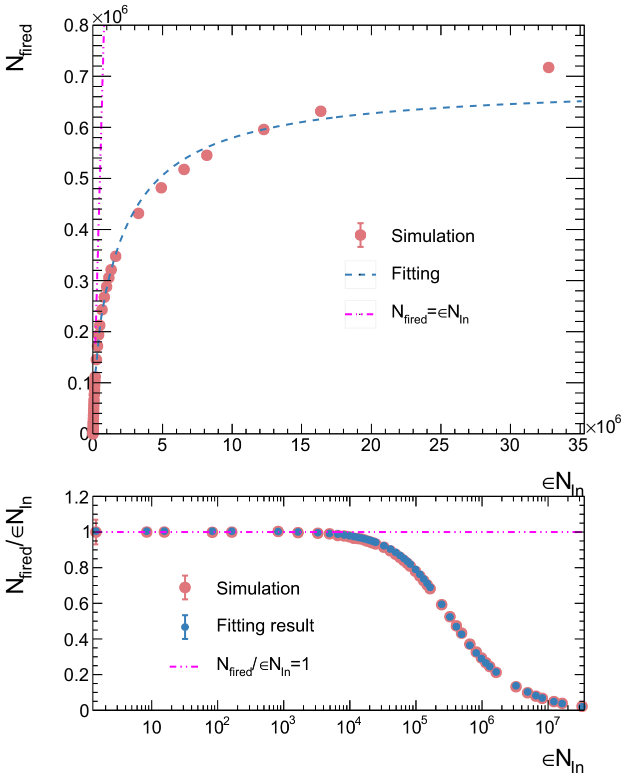

Fig. 13 (Color online) The simulated response of the SiPM to scintillation light from a 2.5 cm×2.5 cm×4 cm LYSO crystal is shown. This SiPM-LYSO setup is identical to that used in the DarkSHINE ECAL. Performance parameters of the SiPM, including PDE, fill factor, pixel pitch, pixel counts, and recovery time, are referenced from the HAMAMATSU S14160-3010PS datasheet [52]. The detected photons exhibit a time structure influenced by the scintillation decay time of LYSO and the geometric effects of the crystal, which are considered in the simulation. The horizontal axis represents the effective photon counts, calculated as the product of the PDE (ϵ) and the number of incident photons (N_{In}). The upper figure displays the variation in the number of photons detected by the SiPM (N_{fired}) as a function of the effective photon counts. The lower figure illustrates the extent to which the response of the SiPM deviates from linearity. It can be observed that for effective photon counts below 10,000, the response of the SiPM remains largely linear. However, as the effective photon count exceeds 10,000, the response begins to deviate from linearity and gradually saturates

6.1.3 ADC digitization

The behavior of the readout electronics was simulated using an ADC digitization process. Table 9 lists the parameters used in this digitization. We assumed that the charge produced by the SiPM is recorded by a 12-bit multichannel analyzer with 4096 ADC counts. Gain is defined as the number of ADC count outputs per photoelectron signal. Three gain modes expand the dynamic range of energy measurements: high gain, medium gain, and low gain. The dynamic energy range for high gain is approximately 0–2.7 MeV, primarily designed for energy calibration using radioactive sources. The maximum energy measured by the designed electronics is approximately 5461 MeV, which exceeds the 4 GeV result presented in Sect. 5. This increase is attributed to a series of smearing effects during digitization that can yield energies greater than the original values. In the high- and medium-gain modes, when the ADC exceeds 4000, it automatically switches to the next gain level. A 3-ADC DAQ noise was set for each gain mode to represent the intrinsic noise. The SiPM noise was set to 1 ADC in high-gain mode and varied with the gain. The digitization model characterizes the SiPM noise as the average dark noise present in each event waveform, accounting for the scintillation decay time of LYSO and the dark count rate of the SiPM. Additionally, a calibration accuracy of 1% was assumed for photoelectron measurements.

6.2 Single-channel performance

After digitization, the ideal energy deposited in the crystal within Geant4 was transformed into a signal that more accurately represented the actual response of the detector. The equivalent noise energy (ENE) for the electronics of the single-channel digitization is shown in Fig. 14a. The ENE was calculated using the following formula:

$$\mathrm{ENE} = \frac{\mathrm{Noise}}{\mathrm{ADC_{p.e.}} \times \mathrm{LY_{mea}}} \tag{1}$$

Table 9 Parameters used in ADC digitization

Modes	Gain	ADC/p.e.	Charge calibration accuracy (%)
High gain	×2000	10	1
Medium gain	×40	0.2	1
Low gain	×1	0.005	1
SiPM noise	DAQ noise	Switching point	Energy range
1 ADC	3 ADC	4000 ADC	0–2.7 MeV
0.02 ADC	3 ADC	4000 ADC	2.7–133.3 MeV
0.0005 ADC	3 ADC	–	133.3-5461 MeV

where Noise represents the number of ADC noise, which includes both SiPM noise and DAQ noise, as listed in Table 9. $ADC_{p.e.}$ is the number of ADC counts per photoelectron, also listed in Table 9. LY_{mea} denotes the number of photoelectrons detected by the SiPM coupled to the crystal when it absorbs 1 MeV of energy. In our setup, LY_{mea} is set to 150 p.e./MeV (Table 7).

In Fig. 14a, the three distinct ENE regions correspond to the different gain modes. Since ENE represents electronic noise and is independent of the input signal, it remains constant across the energy ranges covered by each electronic gain. However, at the transition points between these ranges, the ENE exhibits jumps corresponding to the changes in gain, as do the parameters Noise and $ADC_{p.e.}$.

The single-channel energy resolution, after incorporating the three digitization effects, is shown in Fig. 14b. We individually simulated the digitization process for each component to obtain its respective resolution, followed by a simulation of the combined process to determine the overall resolution. Scintillation digitization involves Poisson sampling based on the intrinsic light yield of the LYSO crystal, along with a series of Gaussian samplings. Consequently, this component of the energy resolution decreases with increasing incident energy. However, due to the high intrinsic light yield of the crystal, this change is not significantly noticeable in Fig. 14b; instead, it is dominated by the constant term introduced by Gaussian sampling, reflecting the calibration accuracy. The resolution of SiPM digitization also decreases with increasing energy. However, because statistical sampling is based on the number of detected photoelectrons—significantly lower than the number of generated scintillation photons due to attenuation and the PDE of the SiPM—the resolution of SiPM digitization is worse than that of scintillation digitization. Moreover, applying a nonlinearity correction further degrades the resolution, as the correction process introduces additional fluctuations. For ADC digitization, the energy resolution shows two jumps at 5 MeV and 500 MeV, attributed to an increase in ENE due to gain switching. Additionally, a constant term appeared in the high-energy region, reflecting the calibration accuracy assumed in the model. Overall, at lower energies (less than 100 MeV), the resolution of SiPM digitization was the main contributor. At higher energies, the contributions from scintillation digitization and ADC digitization became more significant.

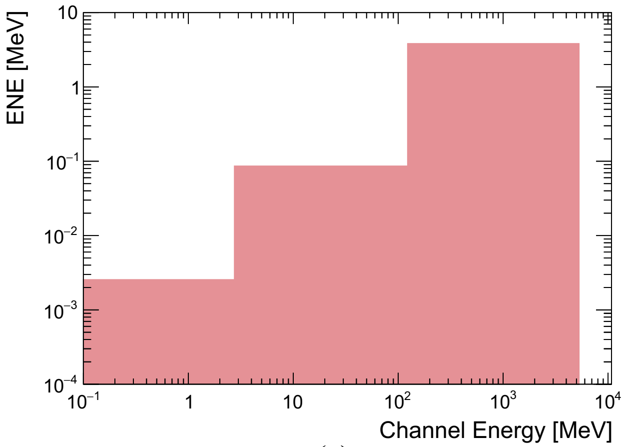

(a)

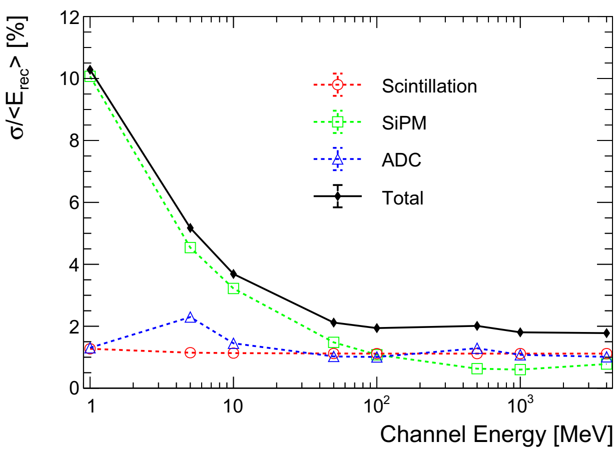

(b)

Fig. 14 (Color online) **a** ENE of a single channel. The *x*-axis represents the input energy in the digitization model, while the y-axis indicates the ENE. The three bins correspond to the three gain modes, each with a fixed ENE value that is independent of input energy. The width of each bin represents the dynamic range of energy measurement at that gain. **b** Energy resolution of a single channel. The *x*-axis represents the input energy in the digitization model, and the *y*-axis indicates the energy resolution of the channel, calculated as the ratio of the standard deviation (σ) to the mean value from a Gaussian fit of the output energy distribution. At energies below 100 MeV, the primary contributor to resolution is the SiPM digitization, which depends on the efficiencies of light collection and photon detection, introducing larger fluctuations in Monte Carlo sampling compared to intrinsic light output and ADC noise. As energy increases, the scintillation digitization and ADC digitization become more dominant, mainly due to constant terms reflecting calibration accuracy

The energy resolutions presented in Fig. 14b were derived from the parameters listed in Tables 7, 8, 9, which correspond to preliminary experimental measurements. Optimizing the LYSO-SiPM units, such as improving light-collection efficiency to achieve a larger light output, could enhance channel resolution.

6.3 ECAL performance

The performance of the full detector was determined by applying digitization to each channel. Figure 15 shows the energy resolution and containment of the ECAL. Here, E_{Truth} denotes the energy of the incident electrons. In the simulation, the ECAL consists of a grid of 21×21×11 LYSO crystals, each with a volume of 2.5 cm×2.5 cm×4 cm, consistent with the results presented in Sect. 4. Targets and other detectors were excluded from this assessment. The incident particles were electrons with energies ranging from 1 GeV to 8 GeV, impacting the front face of the ECAL within a circular area of 3 cm radius.

The energy resolution is plotted at the top of Fig. 15. After digitization, the statistical term of the energy resolution of the ECAL remained better than 2% due to the high intrinsic light yield of the LYSO crystal. This high-energy resolution allows for more precise measurements of recoil electron energy and enhances the reliability of distinguishing between signal and background. The overall energy resolution of the ECAL is typically better than that of a single channel (Fig. 14b) due to statistical averaging, where uncertainties from individual channels tend to cancel out, and energy sharing across multiple channels reduces the impact of measurement errors. Additionally, variations in the responses of different channels are compensated for when combined, thereby improving the overall resolution.

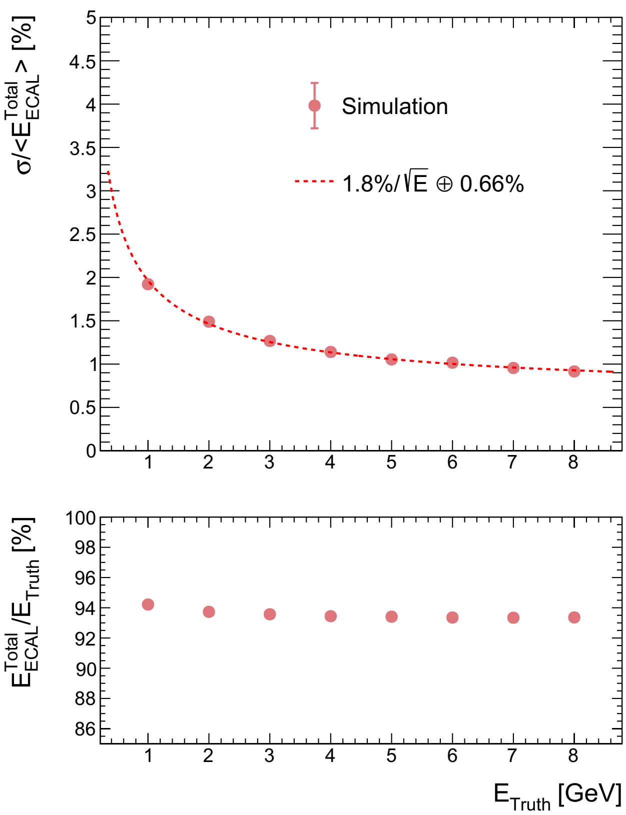

Fig. 15 (Color online) Energy resolution and containment of the ECAL for incident electrons with energies ranging from 1 to 8 GeV, excluding targets and other detectors. The x-axis represents the energy of the incident electrons. The upper figure displays the energy resolution of the ECAL, with the fitted stochastic term achieving better than 2%. The lower figure illustrates the energy containment, defined as the ratio of the energy deposited in the ECAL to the incident energy

The bottom part of Fig. 15 shows the energy containment of the ECAL, defined as the ratio of the energy deposited in the ECAL to the incident energy. The energy containment was less than 100% mainly because a small portion of the energy was deposited in passive materials outside the crystals, such as reflective films, PCBs, and support structures, which could not be detected.

The performance of the ECAL is influenced by the digitization model, which is based on preliminary experimental results from a specific setup. Optimizing the detector configuration can alter the performance; however, the key objective is to develop a tool that accurately evaluates the performance of a detector, bringing it closer to that of a real detector.

7 Radiation damage

Given the high-energy and high-frequency beam environment, the ECAL, particularly its central region, is subjected to significant radiation doses that may degrade its performance. Therefore, evaluating radiation damage to the ECAL is essential, with a focus on ionizing energy loss in the crystals and non-ionizing energy loss causing damage to the silicon sensors. Simulations conducted in Geant4 estimated the radiation damage to the crystals and silicon sensors under conditions corresponding to 3×10^{14} electron-on-target events, which represents one year of operation at a repetition rate of 10 MHz.

Radiation damage to the crystals primarily results from the loss of ionizing energy from incident particles, which is evaluated using the total ionizing dose (TID). The TID of a crystal is defined as the ionizing energy absorbed per unit mass. The average ionizing energy loss absorbed by each crystal in the ECAL was calculated based on one million electron-on-target events. This average value was then multiplied by 3×10^{14} to estimate the TID for each crystal after one year of operation. The maximum TID absorbed by the crystals was approximately 10^7 rad (Fig. 16a). Most inorganic scintillators commonly used in high-energy physics detectors, such as CSI, BGO, and PWO, experience significant light yield loss after exposure to such doses. However, LYSO exhibits only a slight reduction in light yield [56], meeting the radiation resistance requirements of the DarkSHINE ECAL.

Radiation damage to silicon sensors primarily results from non-ionizing energy loss (NIEL), which is typically expressed as an equivalent neutron flux of 1 MeV. To determine the neutron flux on each sensor, the average NIEL per event for each sensor was first calculated through simulation, referred to as E_1. Next, the average NIEL for a 1 MeV neutron passing through a single sensor was simulated as

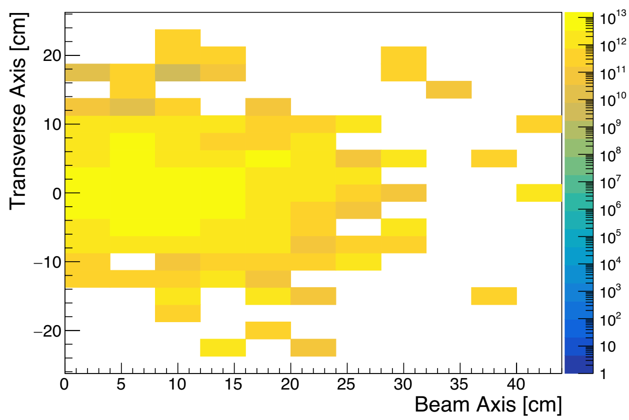

Fig. 16 (Color online) Distribution of radiation damage in the ECAL region under 3×10^{14} electrons-on-target events, corresponding to one year of operation at a 10 MHz repetition rate. The two distributions illustrate radiation damage along the ECAL symmetry plane in the beam direction. The horizontal axis represents the beam direction, while the vertical axis corresponds to the transverse directions, with each segment indicating the position of a crystal. **a** TID absorbed by the crystals, with a maximum value of 10^7 rad. **b** NIEL in the silicon sensors, expressed as the equivalent 1 MeV neutron flux, with a maximum value of 10^{13} per square centimeter

E_2. The ratio E_1/E_2 then provides the equivalent 1 MeV neutron flux for each sensor. In the DarkSHINE ECAL, the equivalent 1 MeV neutron flux on silicon sensors in the most irradiated area is approximately 10^{13} per square centimeter (Fig. 16b). Such radiation level can cause the dark current of typical sensors to increase by several orders of magnitude, rendering them unusable. Therefore, silicon sensors with high-radiation resistance are required for our experiments [57–59].

8 Conclusion

This paper presents the design and optimization of a LYSO crystal ECAL for the DarkSHINE experiment, which aims to detect dark photons as potential candidates for dark force mediators. Comprehensive simulations were conducted to optimize the structure of the ECAL and evaluate its key performance metrics.

The final ECAL design consists of 21×21×11 LYSO crystals, each measuring 2.5 cm×2.5 cm×4 cm, arranged in a staggered configuration to enhance detection efficiency. Both the transverse and longitudinal dimensions of the ECAL were optimized to maximize signal collection while maintaining cost efficiency. A dynamic energy range of 4 GeV was established for each channel to ensure accurate energy measurements without saturation, crucial for background rejection and precise signal detection.

A dedicated digitization model was developed to parameterize the scintillation, SiPM, and ADC behaviors, providing a realistic representation of the detector's performance. This model enabled a detailed analysis of the energy resolution and containment of the ECAL, demonstrating that the statistical term of the energy resolution can achieve better than 2% accuracy due to the high intrinsic light yield of the LYSO crystals.

Radiation damage was thoroughly assessed, estimating the TID absorbed by the crystals and the NIEL in the silicon sensors for one year of operation at a 10 MHz repetition rate. Due to its minimal light-yield reduction under high-radiation doses, LYSO crystal is identified as an ideal scintillator material for the DarkSHINE experiment. In addition, the selected silicon sensors for the ECAL must exhibit high resistance to radiation-induced damage, which is critical for maintaining detector performance in the high-radiation environment anticipated for the experiment.

Author Contributions All authors contributed to the study conception and design. Material preparation, data collection, and analysis were performed by Zhi-Yu Zhao, Qi-Bin Liu, Ji-Yuan Chen, and Shu Li. The first draft of the manuscript was written by Zhi-Yu Zhao, and all authors commented on previous versions of the manuscript. All authors read and approved the final manuscript.

Declarations

Conflict of interest The authors declare that they have no conflict of interest.

References

1. D. Hooper, D.P. Finkbeiner, G. Dobler, Possible evidence for dark matter annihilations from the excess microwave emission around the center of the Galaxy seen by the Wilkinson Microwave Anisotropy Probe. Phys. Rev. D **76**, 083012 (2007). https://doi.org/10.1103/PhysRevD.76.083012
2. D. Clowe, M. Bradac, A.H. Gonzalez et al., A direct empirical proof of the existence of dark matter. Astrophys. J. Lett. **648**, L109–L113 (2006). https://doi.org/10.1086/508162
3. Y. Du, F. Huang, H.L. Li et al., Revisiting dark matter freeze-in and freeze-out through phase-space distribution. JCAP **04**, 012 (2022). https://doi.org/10.1088/1475-7516/2022/04/012
4. E. Aprile, K. Abe, F. Agostini et al., First dark matter search with nuclear recoils from the XENONnT experiment. Phys. Rev. Lett. **131**, 041003 (2023). https://doi.org/10.1103/PhysRevLett.131.041003
5. Y. Meng, Z. Wang, Y. Tao et al., Dark matter search results from the PandaX-4T commissioning run. Phys. Rev. Lett. **127**, 261802 (2023). https://doi.org/10.1103/PhysRevLett.127.261802
6. Y. Wang, Z. Zeng, Q. Yue et al., First experimental constraints on WIMP couplings in the effective field theory framework from CDEX. Sci. China. Phys. Mech. Astron. **64**, 281011 (2021). https://doi.org/10.1007/s11433-020-1666-8
7. J. Aalbers, D.S. Akerib, C.W. Akerlof et al., First dark matter search results from the LUX-ZEPLIN (LZ) experiment. Phys. Rev.

Lett. **131**, 041002 (2023). https://doi.org/10.1103/PhysRevLett.131.041002

8. F. Giovacchini, J. Casaus, A. Oliva et al., The AMS-02 RICH detector: status and physics results. Nucl. Instrum. Meth. A **952**, 161797 (2020). https://doi.org/10.1016/j.nima.2019.01.024
9. D. Kyratzis, Results overview from the DAMPE space mission in orbit. PoS PANIC2021, 310 (2022). https://doi.org/10.22323/1.380.0310
10. G. Stefano, WIMP dark matter searches with the ATLAS detector at the LHC. Front. Phys. **7**, 75 (2019). https://doi.org/10.3389/fphy.2019.00075
11. K. Griest, M. Kamionkowski, Unitarity limits on the mass and radius of dark matter particles. Phys. Rev. Lett. **64**, 615 (1990). https://doi.org/10.1103/PhysRevLett.64.615
12. C.M. Ho, R.J. Scherrer, Limits on MeV dark matter from the effective number of neutrinos. Phys. Rev. D **87**, 023505 (2013). https://doi.org/10.1103/PhysRevD.87.023505
13. G. Steigman, Equivalent neutrinos, light WIMPs, and the chimera of dark radiation. Phys. Rev. D **87**, 103517 (2013). https://doi.org/10.1103/PhysRevD.87.103517
14. C. Boehm, M.J. Dolan, C. McCabe, A lower bound on the mass of cold thermal dark matter from Planck. JCAP **08**, 041 (2013). https://doi.org/10.1088/1475-7516/2013/08/041
15. K.M. Nollett, G. Steigman, BBN and the CMB constrain light, electromagnetically coupled WIMPs. Phys. Rev. D **89**, 083508 (2014). https://doi.org/10.1103/PhysRevD.89.083508
16. K.M. Nollett, G. Steigman, BBN and the CMB constrain neutrino coupled light WIMPs. Phys. Rev. D **91**, 083505 (2015). https://doi.org/10.1103/PhysRevD.91.083505
17. P.D. Serpico, G.G. Raffelt, MeV-mass dark matter and primordial nucleosynthesis. Phys. Rev. D **70**, 043526 (2004). https://doi.org/10.1103/PhysRevD.70.043526
18. J. Billard, M. Boulay, S. Cebrián et al., Direct detection of dark matter—APPEC committee report*. Rept. Prog. Phys. **85**, 056201 (2022). https://doi.org/10.1088/1361-6633/ac5754
19. B. Holdom, Two U(1)'s and epsilon charge shifts. Phys. Lett. B **166**, 196–198 (1986). https://doi.org/10.1016/0370-2693(86)91377-8
20. R. Foot, X.G. He, Comment on Z Z′ mixing in extended gauge theories. Phys. Lett. B **267**, 509–512 (1991). https://doi.org/10.1016/0370-2693(91)90901-2
21. K. Fuyuto, X.G. He, G. Li et al., CP-violating dark photon interaction. Phys. Rev. D **101**, 075016 (2020). https://doi.org/10.1103/PhysRevD.101.075016
22. G. Choi, T.T. Yanagida, N. Yokozaki, A model of interacting dark matter and dark radiation for H_0 and σ_8 tensions. JHEP **01**, 127 (2021). https://doi.org/10.1007/JHEP01(2021)127
23. Y. Cheng, X.G. He, M. Ramsey-Musolf et al., CP violating dark photon kinetic mixing and type-III seesaw model. Phys. Rev. D **105**, 095010 (2022). https://doi.org/10.1103/physrevd.105.095010
24. D. Banerjee, V.E. Burtsev, A.G. Chumakov et al., Dark matter search in missing energy events with NA64. Phys. Rev. Lett. **123**, 121801 (2019). https://doi.org/10.1103/PhysRevLett.123.121801
25. H. Abreu, J. Anders, C. Antel et al., [FASER Collaboration], Search for dark photons with the FASER detector at the LHC. Phys. Lett. B **848**, 138378 (2024). https://doi.org/10.1016/j.physletb.2023.138378
26. F. Abudinén, I. Adachi, L. Aggarwal et al., Search for a dark photon and an invisible dark Higgs Boson in $\mu^+\mu^-$ and missing energy final states with the Belle II experiment. Phys. Rev. Lett. **130**, 071804 (2023). https://doi.org/10.1103/PhysRevLett.130.071804
27. Y. Zhang, W.T. Zhang, M. Song et al., Probing invisible decay of a dark photon at BESIII and a future Super Tau Charm Factory via monophoton searches. Phys. Rev. D **100**, 115016 (2019). https://doi.org/10.1103/PhysRevD.100.115016
28. V. Prasad, Dark matter/ new physics searches at BESIII. PoS **ALPS2019**, 030 (2020). https://doi.org/10.22323/1.360.0030
29. M. Fabbrichesi, E. Gabrielli, G. Lanfranchi, *The Physics of the Dark Photon: A Primer* (Springer, Berlin, 2021). https://doi.org/10.1007/978-3-030-62519-1
30. T. Åkesson et al. [LDMX], Light dark matter eXperiment (LDMX). [arXiv:1808.05219 [hep-ex]]
31. T. Åkesson et al., [LDMX], A high efficiency photon veto for the light dark matter eXperiment. JHEP **04**, 003 (2020). https://doi.org/10.1007/JHEP04(2020)003
32. A. Berlin, N. Blinov, G. Krnjaic et al., Dark matter, millicharges, axion and scalar particles, gauge osons, and other new physics with LDMX. Phys. Rev. D **99**, 075001 (2019). https://doi.org/10.1103/PhysRevD.99.075001
33. J. Chen, J.Y. Chen, J.F. Chen et al., Prospective study of light dark matter search with a newly proposed DarkSHINE experiment. Sci. China Phys. Mech. Astron. **66**, 211062 (2023). https://doi.org/10.1007/s11433-022-1983-8
34. S. Li, Dark SHINE - a dark photon search initiative at SHINE facility. in *Proceeding for 31st International Symposium on Lepton Photon Interactions at High Energies*. https://doi.org/10.5281/zenodo.8373963
35. J. Wan, Y. Leng, B. Gao et al., Simulation of wire scanner for high repetition free electron laser facilities. Nucl. Instrum. Meth. A **1026**, 166200 (2022). https://doi.org/10.1016/j.nima.2021.166200
36. Z.T. Zhao, C. Feng, K.Q. Zhang, Two-stage EEHG for coherent hard X-ray generation based on a superconducting linac. Nucl. Sci. Tech. **28**, 117 (2017). https://doi.org/10.1007/s41365-017-0258-z
37. T. Kimble, M. Chou, B.H.T. Chai, Scintillation properties of LYSO crystals. IEEE. Nucl. Sci. Symposium Conf. Rec. Norfolk, VA, USA, **3**, 1434–1437 (2002). https://doi.org/10.1109/NSSMIC.2002.1239590
38. J. N. Butler, [CMS Collaboration], A MIP Timing Detector for the CMS Phase-2 Upgrade. CERN, CERN-LHCC-2019-003, CMS-TDR-020 (2019)
39. V. Kalinnikov, E. Velicheva, A. Rozhdestvensky, Measurement of the LYSO: Ce and LYSO:Ce, Ca scintillator response for the electromagnetic calorimeter of the COMET experiment. Phys. Part. Nucl. Lett. **20**, 995–1001 (2023). https://doi.org/10.1134/S1547477123050412
40. R. Klanner, Characterisation of SiPMs. Nucl. Instrum. Meth. A **926**, 36–56 (2019). https://doi.org/10.1016/j.nima.2018.11.083
41. F. Simon, Silicon photomultipliers in particle and nuclear physics. Nucl. Instrum. Meth. A **926**, 85–100 (2019). https://doi.org/10.1016/j.nima.2018.11.042
42. X. Z. Yu, X. Y. Wang, W. H. Ma, et al., Production and test of sPHENIX W/SciFiber electromagnetic calorimeter blocks in China. Nucl. Sci. Tech. **35**(8), 145 (2024) https://doi.org/10.1007/s41365-024-01517-y
43. Y. Xu, Y. S. Ning, Z. Z. Qin, et al., Development of a scintillating-fiber-based beam monitor for the coherent muon-to-electron transition experiment. Nucl. Sci. Tech. **35**(4), 79 (2024) https://doi.org/10.1007/s41365-024-01442-0
44. S. Agostinelli, J. Allison, K. Amako et al., GEANT4-a simulation toolkit. Nucl. Instrum. Meth. A **506**, 250–303 (2003). https://doi.org/10.1016/S0168-9002(03)01368-8
45. J. Zhu, X. Peng, S. Luo, et al., Performance of the electromagnetic calorimeter module in the NICA-MPD based on Geant4. Nucl. Sci. Tech. (in Chinese) **46**(12), 120202 (2023) https://doi.org/10.11889/j.0253-3219.2023.hjs.46.120202
46. E. Izaguirre, G. Krnjaic, P. Schuster et al., Testing GeV-scale dark matter with fixed-target missing momentum experiments. Phys. Rev. D **91**, 094026 (2015). https://doi.org/10.1103/PhysRevD.91.094026

47. Z. Wang, R. Yuan, H.Q. Liu et al., A design of hadronic calorimeter for DarkSHINE experiment. Nucl. Sci. Tech. **35**, 148 (2024). https://doi.org/10.1007/s41365-024-01502-5
48. Y. H. Guo, S. Li, K. Liu, et al., Design of high-speed readout electronics for the DarkSHINE electromagnetic calorimeter. [arXiv:2407.20723 [physics.ins-det]]
49. J. Y. Zhu, Y. Z. Su, H. B. Yang, et al., Design and prototyping of the readout electronics for the transition radiation detector in the high energy cosmic radiation detection facility. Nucl. Sci. Tech. **35**, 82 (2024). https://doi.org/10.1007/s41365-024-01446-w
50. Y. Li, C. Li, K. Hu, et al., Design and development of multi-channel front end electronics based on dual-polarity charge-to-digital converter for SiPM detector applications. Nucl. Sci. Tech. **34**, 18 (2023). https://doi.org/10.1007/s41365-023-01168-5
51. Z. Y. Zhao, B. H. Qi, S. Li, et al., Dynamic Range of SiPMs with high pixel densities. [arXiv:2407.17794 [physics.ins-det]]
52. HAHAMATSU, S4160-3010PS. https://www.hamamatsu.com.cn/cn/zh-cn/product/optical-sensors/mppc/mppc_mppc-array/S14160-3010PS.html
53. K. Kotera, W. Choi, T. Takeshita, Describing the response of saturated SiPMs. [arXiv:1510.01102 [physics.ins-det]]
54. C. Piemonte, A. Gola, Overview on the main parameters and technology of modern silicon photomultipliers. Nucl. Instrum. Meth. A **926**, 2–15 (2019). https://doi.org/10.1016/j.nima.2018.11.119
55. F. Nagy, M. Mazzillo, L. Renna et al., Afterpulse and delayed crosstalk analysis on a STMicroelectronics silicon photomultiplier. Nucl. Instrum. Meth. A **759**, 44–49 (2014). https://doi.org/10.1016/j.nima.2014.04.045
56. R. Y. Zhu, Ultrafast and radiation hard inorganic scintillators for future HEP experiments. J. Phys. Conf. Ser. **1162**, 012022 (2019). https://doi.org/10.1088/1742-6596/1162/1/012022
57. A. Ulyanov, D. Murphy, J. Mangan, et al., Radiation damage study of SensL J-Series silicon photomultipliers using 101.4 MeV protons. Nucl. Instrum. Meth. A **976**, 164203 (2020). https://doi.org/10.1016/j.nima.2020.164203
58. S. Sanchez Majos, P. Achenbach, C. Ayerbe Gayoso, et al., Noise and radiation damage in silicon photomultipliers exposed to electromagnetic and hadronic radiation. Nucl. Instrum. Meth. A **602**, 506–510 (2009). https://doi.org/10.1016/j.nima.2009.01.176
59. R. Preghenella, M. Alexeev, P. Antonioli, et al., A SiPM-based optical readout system for the EIC dual-radiator RICH. Nucl. Instrum. Meth. A **1046**, 167661 (2023). https://doi.org/10.1016/j.nima.2022.167661

Authors and Affiliations

Zhi-Yu Zhao[1,2,3] · Qi-Bin Liu[1,2,3] · Ji-Yuan Chen[1,2,3] · Jing Chen[1,2,3] · Jun-Feng Chen[4,5] · Xiang Chen[2,3] · Chang-Bo Fu[6,7] · Jun Guo[2,3] · Kim Siang Khaw[1,2,3] · Liang Li[2,3] · Shu Li[1,2,3] · Dan-Ning Liu[1,2,3] · Kun Liu[1,2,3] · Si-Yuan Song[1,2,3] · Tong Sun[1,2,3] · Jian-Nan Tang[2,3] · Yu-Feng Wang[1,2,3] · Zhen Wang[1,2,3] · Wei-Hao Wu[2,3] · Hai-Jun Yang[1,2,3] · Yu-Ming Lin[1,2,3] · Rui Yuan[1,2,3] · Yu-Lei Zhang[2,3] · Yun-Long Zhang[8,9] · Bai-Hong Zhou[1,2,3] · Xu-Liang Zhu[1,2,3] · Yi-Fan Zhu[1,2,3]

✉ Shu Li
shuli@sjtu.edu.cn

1 Tsung-Dao Lee Institute, Shanghai Jiao Tong University, 1 Lisuo Road, Shanghai 201210, China

2 Institute of Nuclear and Particle Physics, School of Physics and Astronomy, 800 Dongchuan Road, Shanghai 200240, China

3 Key Laboratory for Particle Astrophysics and Cosmology (MOE), Shanghai Key Laboratory for Particle Physics and Cosmology (SKLPPC), Shanghai Jiao Tong University, 800 Dongchuan Road, Shanghai 200240, China

4 Center of Materials Science and Optoelectronics Engineering, University of Chinese Academy of Sciences, Beijing 100049, China

5 Shanghai Institute of Ceramics, Chinese Academy of Sciences, Shanghai 201899, China

6 Key Laboratory of Nuclear Physics and Ion-beam Application (MOE), Fudan University, Shanghai 200443, China

7 Institute of Modern Physics, Fudan University, Shanghai 200443, China

8 State Key Laboratory of Particle Detection and Electronics, University of Science and Technology of China, Hefei 230026, China

9 Department of Modern Physics, University of Science and Technology of China, Hefei 230026, China